

Articulated 3D Human-Object Interactions From RGB Videos: An Empirical Analysis of Approaches and Challenges

Sanjay Haresh, Xiaohao Sun, Hanxiao Jiang, Angel X. Chang, Manolis Savva

Simon Fraser University

3dlg-hcvc.github.io/3dhoi

Abstract

Human-object interactions with articulated objects are common in everyday life. Despite much progress in single-view 3D reconstruction, it is still challenging to infer an articulated 3D object model from an RGB video showing a person manipulating the object. We canonicalize the task of articulated 3D human-object interaction reconstruction from RGB video, and carry out a systematic benchmark of five families of methods for this task: 3D plane estimation, 3D cuboid estimation, CAD model fitting, implicit field fitting, and free-form mesh fitting. Our experiments show that all methods struggle to obtain high accuracy results even when provided ground truth information about the observed objects. We identify key factors which make the task challenging and suggest directions for future work on this challenging 3D computer vision task.

1. Introduction

Indoor environments contain many articulated objects with which we interact on a daily basis. Doors, kitchen cabinetry, fridges, and drawers are but a few examples. Thus, a comprehensive 3D understanding of the world requires modeling how people interact with articulated objects.

There has been much recent progress in dynamic 3D reconstruction targeting humans [5, 15, 26, 30], animals [49–51], and objects [41, 45–47]. There is also increasing interest in whole-body human-object interactions (HOI) in 3D [3, 43, 48]. However, this line of work assumes static scenarios [43, 48], or assumes the object is not articulated [3].

There is much less work on modeling 3D HOI with articulated household objects (e.g. ‘opening a microwave’). Such scenarios exhibit many challenges. Firstly, both the person and articulating object are moving and changing in appearance. Moreover, even though the object may articulate many household objects such as furniture and appliances, are themselves not easily movable. This coupled with typically limited viewpoints for such interaction scenarios leads to

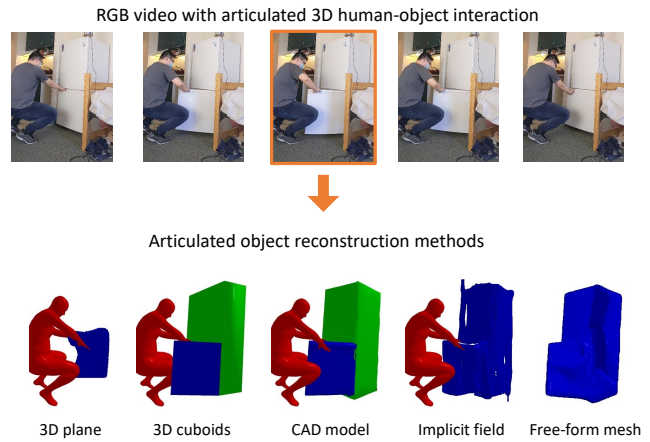


Figure 1. We address the articulated 3D human-object interaction task. Given an input RGB video, methods tackling this task output a 3D representation of an articulated object manipulated by a human. This is a challenging task requiring 3D object reconstruction under severe occlusion, as well as part motion estimation. We systematically benchmark methods using a spectrum of representations for the articulated object ranging from simple planes and cuboids to CAD models, implicit fields, and free-form meshes.

significant occlusions between the object and the human, and in particular very partial observations of the object (e.g., the back of a fridge is rarely observed, see Figure 1). Thus inference of 3D HOI with articulated objects from monocular RGB video is a challenging problem, especially as there is limited ground truth data for supervision.

While there are challenges in modeling articulated 3D HOI, there are also opportunities. Many common objects with which people interact are composed of rigid parts, and can be abstracted to simple primitive shapes. For instance, 3DADN [31] recently simplified the articulated 3D HOI problem to a single 3D plane estimation for a moving part such as a microwave oven door. Xu et al. [44] introduced a dataset of RGB videos of 3D HOI with articulated objects, and demonstrated that the human pose can be used to refine the articulated object reconstruction. Additional physical constraints and priors connecting the static and moving parts

of objects and the moving human body can likely enable even better articulated 3D HOI reconstruction.

In this paper, we define and canonicalize the “RGB video to articulated 3D HOI” task. Our goal is to analyze the performance of recent techniques for direct reconstruction of 3D articulated objects from RGB video. To this end, we systematically benchmark five families of techniques: plane estimation, cuboid abstraction, CAD model fitting, implicit fields, and freeform mesh fitting. We find that even with access to ground truth information all methods struggle to obtain high quality results especially when considering motion parameter estimation for articulated parts. Direct optimization methods using cuboidal abstractions or CAD models perform relatively well compared to more complex approaches, but in the latter case are limited by needing a dataset of CAD models matching the input videos.

2. Related Work

3D articulated object reconstruction. There has been growing interest in reconstructing 3D articulated objects i.e. objects with moving parts such as drawers and doors. Earlier work focused on using probabilistic models for modeling articulated objects as kinematic graphs [34, 35]. Other work predicted part poses [25] and articulation parameters [16, 24, 27], and reconstructed objects that can be articulated from partial 3D point clouds [19, 28]. Recent work has employed radiance fields to model articulated objects [36]. The above work typically operates on largely unoccluded views of a single object of interest. Such views are quite dissimilar from real-world videos of human interaction with common household objects, where clearly the object does not typically articulate on its own. Our task focuses on reconstructing a 3D articulated object from RGB videos of natural interactions involving both human and object.

Monocular 3D articulated objects from RGB video. We focus on single-view RGB video input as it is ubiquitous and captures the inherent temporal nature of motion by the human causing the object articulation. Despite this fact, there is little prior work taking advantage of the temporal nature of articulation. Some existing work relies on sequences of depth frames [16, 17] or estimated depth frames [25]. Methods that estimate 3D articulated objects from RGB video tend to assume predetermined articulation structure (e.g., human, four-legged animal) [4, 21]. More recent methods [41, 45–47] have explored category-agnostic articulated object reconstruction. There has also been work that discovers parts and joints from multiview video [29]. We focus on reconstructing a 3D model of an articulated object from a single fixed-view RGB video, during a natural interaction involving a human manipulating the object.

3D human object interaction. While there is a long line of work on 2D human-object interaction (see recent sur-

vey by Bergstrom and Shi [2]), there is much less work on 3D human-object interaction. Some work deals with hand-object interactions [6, 13] typically focusing on estimating hand pose for manipulations of rigid objects. There has been some recent work on hand interactions with deformable objects [37] and with articulated objects [10]. We focus on full-body interactions with common household furniture and appliances. Considering full-body 3D HOI there has been work on exploiting human-object constraints to model object arrangements [11, 18], populate humans in scenes [12] and to recover human object arrangements in 3D [33]. Zhang et al. [48] presented an optimization-based method to recover static human and object arrangements in 3D from a single RGB image. Bhatnagar et al. [3] infer 3D HOI from RGB videos. More recently, Xie et al. [43] handle dynamic interactions but again with non-articulating objects. None of this work on full-body 3D HOI work handles articulated objects. In contrast, Xu et al. [44] proposed to exploit human-object constraints to reconstruct 3D articulated objects from videos of 3D HOI. Like Zhang et al. [48], this work requires predefined category-level information in the form of CAD models for each object category. Qian et al. [31] estimate a 3D plane for the moving part of an articulating object in a 3D HOI video. In this paper, we systematically benchmark representative methods from these recent approaches for articulated 3D HOI on a standardized task definition and dataset.

3. Task Problem Statement

Here, we define our task. Given a single-view fixed-viewpoint RGB video with N frames $X = \{x_1, x_2, \dots, x_N\}$ showing a human interacting with an object, we reconstruct an articulated model of the object capturing the shape S , pose $P = \{R, T, \sigma\}$, and articulation parameters A_t at each timestamp t . The object shape S includes both the static parts of the object and a moving part that articulates according to A_t . The object pose is parameterized by a rotation R , translation T , and scale σ . The motion parameters $A_t = \{c_t, d_t, \alpha_t\}$ are composed of the motion axis origin $c_t \in \mathbb{R}^3$, motion axis direction $d_t \in \mathbb{R}^3$ (we also evaluate a directionless motion axis a_t), and motion state α_t . For simplicity we assume that the object is stationary so there is a single motion axis (i.e. c, d, a are constant across t). In this work, we restrict our study to rotational motion, and define α_t to be the rotated angle from the closed state. For consistency, we define positive angles to be counterclockwise about the motion axis direction. We measure task performance along three axes:

- **Reconstruction:** the object shape S should accurately represent the object in the video.
- **Pose:** the inferred 3D pose of the object $P = \{R, T, \sigma\}$ should match the input video.
- **Motion:** the moving parts of S should have accurate articulation parameters A_t .

The task defined above is challenging because: i) no 3D supervision is assumed and therefore the problem is highly under-constrained; and ii) we do not assume any category-level information for the objects (i.e. the objects being reconstructed are not known a priori). This significantly increases the space of possible reconstructions. Note that even though the video input includes a human actor, and modeling the human may be beneficial to methods tackling this task, we do not evaluate human pose estimation or mesh reconstruction.

4. Methods

Our goal is to benchmark different approaches for reconstructing an articulated 3D object from an RGB video of a human interacting with the object. We pick representative methods that span a spectrum of output 3D representations types: 3D planes, 3D cuboids, CAD models, implicit fields, and free-form meshes. This spectrum reconstructs the object with 3D representations ranging from “low-fidelity” to “high-fidelity”.

4.1. 3D Plane Estimation

Qian et al. [31] propose the *3D Articulation Detection Network* (3DADN) to detect the articulating part and estimate a 3D plane for it given an RGB video of a human manipulating an object as input. Articulating part detection is done with a Mask R-CNN [14] architecture that is trained on internet videos to regress a part bounding box and motion axis. A part plane regression head and mask head are finetuned using ScanNet [8] scenes augmented with virtual humans. Then, a temporal optimization refines per-frame predictions across the video to improve motion axis consistency and compute motion values (i.e. rotation angles).

We adapt 3DADN to our task by making the following modifications. First, we approximate the moving part as a cuboid, which we obtain by extruding the estimated 3D plane along the plane normal by 5 cm. Since 3DADN does not estimate the static part of the object, we use the moving part as a proxy for the entire shape S . Second, the original 3DADN method assumes monotonically increasing or decreasing motion parameters in an input video (i.e. only opening or closing motion). Thus, we split input videos into parts containing only one type of motion (using the ground truth motion annotation), apply 3DADN to each part and recombine the output into a single sequence. Finally, since we use a pretrained 3DADN, we adjust input videos to match the field-of-view of its training dataset through central cropping and padding. Since 3DADN provides per-frame estimates of the motion axis and origin, we select the median of the predicted axes to obtain a consistent axis for all the frames.

4.2. 3D Cuboid Estimation

Our cuboid-based abstraction baseline CUBEOPT represents each articulated object with two cuboids, $S =$

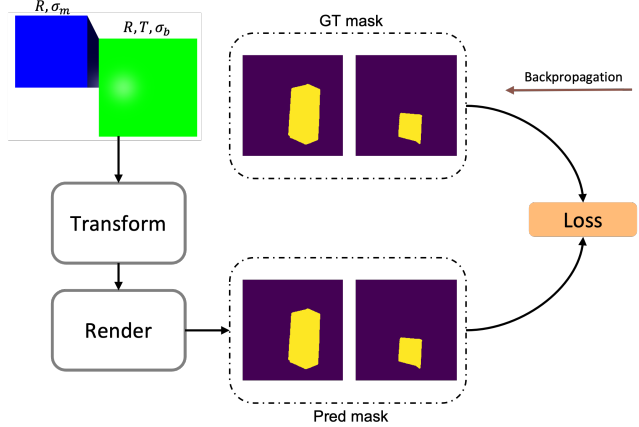


Figure 2. CUBEOPT overview. We recover R , T , σ_b and σ_m estimates through gradient based optimization by minimizing the discrepancy between predicted object masks and ground truth object masks. We use additional loss terms but do not show them here for simplicity.

$\{C_b, C_m\}$, where C_b represents the static part and C_m represents the moving part of the object. The two cuboids are constrained to have an axis of rotation a_m which coincides with an edge of the base part C_b . Under this constraint, we optimize for a rotation R and translation T for the entire object assembly. Since the two parts can have different sizes, there are scale parameters σ_b and σ_m for the base part and the moving part respectively. Finally, we also optimize for articulation state parameters α_t which give the degree of rotation of the moving part at each timestamp t . Figure 2 provides an overview of the approach. See the supplement for more implementation details.

4.3. CAD Model Fitting

Xu et al. [44] proposed an optimization based approach that reconstructs articulated objects and humans from RGB video. The method adopts an optimization approach similar to CUBEOPT but approximates the object shape S using a CAD model. The pose P and articulation parameters A_t are optimized by minimizing the silhouette discrepancy with object segmentation masks and using human-object interaction terms to constrain the relative position of the human and object in 3D.

We evaluate three variations of the D3DHOI method. The original method uses ground truth CAD models to fit the data which leads to very good results for object shape and articulation reconstruction. However, this is not realistic as we typically cannot assume we have ground truth CAD models for an object observed in the input video at test time. Therefore, we also evaluate two more variations of the method with less ground truth knowledge (and add the suffix “GT-CAD” to the original method name to communicate this privileged information is provided as input):

- **D3DHOI-Rand-Cat-CAD:** Instead of optimizing with the ground truth CAD model we randomly select a model from the same category. Note that while this variant assumes less information than the ground truth CAD model, it is still a strong baseline as it is given the category label of the object in the input video.
- **D3DHOI-Rand-CAD:** We randomly select a CAD model from all available CAD models. This variant is more general as it does not rely on a priori knowledge of the object category. However it is still restricted to the 24 CAD models in the dataset from Xu et al. [44].

4.4. Implicit Fields for Articulated Objects

Implicit field have recently been used for modeling articulated objects [19, 28]. We benchmark DITTO [19], a category-agnostic method for reconstructing articulated objects using implicit fields. DITTO takes as input a pair of point clouds (PCs) of the object before and after interaction (in two different articulation states). The method assumes that the two PCs are in the same pose. To adapt DITTO to our task we project the GT CAD model into each frame using GT pose and camera parameters. We then select one frame that is in the closed state (based on GT states) as the reference PC and iterate through the other frames using the PC obtained from the other frames treat other frames as the second PC. This effectively gives us partial (single-view) GT PCs for each frame. We use DITTO pretrained on the shape2motion [40] dataset and apply it to our dataset. For each frame we obtain a predicted mesh reconstruction, segmentation, and joint parameters. To obtain a consistent estimate of the joint axis and origin we take the median of the frame-wise predictions, similarly to 3DADN and LASR). We then compute the mean errors over all the frames. There are some additional differences between how we use DITTO and how it was used in the original paper, which we discuss in detail in the supplement.

4.5. Free-Form Mesh Fitting

As representatives of free-form 3D mesh fitting we use the LASR [45] and ViSER [46] methods. LASR is based on the classical “analysis by synthesis” approach i.e. instead of learning-based methods that learn a data-driven model using a large dataset, LASR reconstructs objects by overfitting to a single video. It takes a mesh sphere and “morphs” it into the object shape S by optimizing for silhouette, optical flow and texture losses. This approach can work well with video data because videos can provide strong 3D multi-view constraints for a single object (relative to single-view images). Using videos also enables the use of optical flow which provides dense correspondence of features between two images.

LASR also learns the camera parameters jointly with the object reconstruction. We use the predicted camera parameters to compute the object pose parameters. However, we

note that the predicted mesh often does not articulate and the motion in the video is mostly explained by rigid transformations of a largely static object mesh. Moreover, the predicted linear blend skinning weights do not carry semantic meaning making it difficult to create discrete “moving” and “static” parts, and compute the corresponding articulation motion parameters (e.g., axis of rotation). ViSER builds on LASR by learning surface embeddings to establish long range correspondences across video frames. Long-range video pixel correspondences are forced to be consistent with an underlying canonical 3D mesh through embeddings that capture the appearance of each surface point.

While these methods provide good results on reconstruction of moving articulated objects such as animals and people from monocular videos, they struggle to reconstruct unobserved parts of the object. We will see that these approaches fail to perform in our setting of indoor human-object interactions where many of the objects are partially observed.

5. Experiments

5.1. Data

We conduct our experiments on the D3D-HOI dataset [44] which contains 256 RGB videos of a person interacting with nine types of common household objects. We choose this dataset because it provides challenging scenarios of humans interacting with common household objects. It is also the only human-object interaction dataset with fine-grained 3D annotations for the object shape and motion parameters. Each video is annotated with an articulated 3D CAD object which is aligned with the RGB image. In addition, Xu et al. [44] provide an estimated SMPL [26] mesh of the person predicted by running EFT [20]. Using the annotated CAD object we generate object and moving part segmentation masks which we treat as the ground truth segmentation masks in our experiments. We conduct our experiments on eight object categories with revolute motion which amount to a total of 239 videos.

5.2. Metrics

We evaluate the five types of methods by measuring their performance at: 1) object shape reconstruction; 2) object pose estimation; and 3) motion parameter estimation (for the articulating part). For each, we define error metrics and accuracy metrics based on thresholding the errors. All metrics are computed per frame, and then averaged over each video, and then across videos. We adopt Chamfer Distance (CD) for our reconstruction metric [9], and translational, rotational and scale errors as object pose metrics [39, 42]. The motion parameter estimation metrics are based on computing the error for individual motion parameters.

Reconstruction. To evaluate the quality of the reconstructed

Table 1. Error metrics for 3DADN, CUBERAND, CUBEOPT (all losses), D3DHOI and LASR. *indicates that the method has access to the GT object mask (all methods except 3DADN and CUBERAND). In addition, CUBEOPT has access to GT part mask, D3DHOI requires CAD models and DITTO has access to ground-truth depth maps. We see that all methods exhibit fairly high motion parameter errors. LASR exhibits high pose translation and rotation errors.

Method	Reconstruction Error ↓		Pose Error ↓				Motion Error ↓			
	CD (Object)	CD (Moving)	Rotation	Translation	Scale	Origin	Axis	Direction	State	
3DADN [31]	4.51 ± 0.12	0.44 ± 0.04	47.54 ± 1.52	2.10 ± 0.06	0.50 ± 0.01	0.99 ± 0.10	26.64 ± 1.88	111.88 ± 4.48	89.77 ± 21.22	
CUBERAND	1.34 ± 0.04	2.07 ± 0.01	52.45 ± 1.36	3.04 ± 0.09	0.14 ± 0.01	1.48 ± 0.00	60.26 ± 0.00	98.28 ± 0.00	196.20 ± 39.82	
CUBEOPT *	1.57 ± 0.11	0.66 ± 0.06	38.94 ± 1.74	2.37 ± 0.09	0.28 ± 0.01	0.71 ± 0.03	27.42 ± 2.06	94.09 ± 4.53	126.60 ± 5.00	
D3DHOI-GT-CAD [44]*	0.45 ± 0.05	0.15 ± 0.02	17.48 ± 1.04	0.85 ± 0.04	0.15 ± 0.01	0.28 ± 0.02	10.27 ± 0.89	10.27 ± 0.89	16.29 ± 0.77	
D3DHOI-Rand-Cat-CAD*	0.66 ± 0.06	0.35 ± 0.03	24.84 ± 1.53	1.16 ± 0.05	0.18 ± 0.01	0.38 ± 0.02	19.27 ± 1.78	28.91 ± 2.91	24.28 ± 1.07	
D3DHOI-Rand-CAD*	1.90 ± 0.20	0.61 ± 0.04	35.26 ± 1.66	1.78 ± 0.07	0.22 ± 0.01	0.50 ± 0.02	54.30 ± 2.43	85.09 ± 3.34	29.71 ± 0.96	
DITTO [19]	0.65 ± 0.03	1.63 ± 0.06	9.75 ± 0.37	0.97 ± 0.02	0.06 ± 0.00	0.29 ± 0.00	67.57 ± 1.61	87.21 ± 2.16	70.10 ± 1.59	
LASR [45]*	1.19 ± 0.04	1.58 ± 0.05	37.60 ± 1.13	8.42 ± 0.29	0.43 ± 0.02	10.56 ± 0.27	60.07 ± 1.63	92.79 ± 2.53	161.27 ± 4.93	
ViSER [46]*	1.48 ± 0.04	1.71 ± 0.05	49.66 ± 1.51	20.46 ± 0.21	0.61 ± 0.01	20.60 ± 0.37	56.00 ± 1.43	93.53 ± 2.61	188.55 ± 5.22	

Table 2. Accuracy results for 3DADN, CUBERAND, CUBEOPT (all losses), D3DHOI and LASR. *indicates that the method has access to the GT object mask (all methods except 3DADN and CUBERAND). In addition, CUBEOPT has access to GT part mask, D3DHOI requires CAD models and DITTO has access to ground-truth depth maps. Motion accuracies are based on matches for the reconstruction and pose accuracies (i.e. within the error threshold for reconstruction and pose). Overall accuracies are based on matches for all the indicated combinations of parameters. The rotation threshold is 10 degrees, the translation threshold is 0.5, and the scale threshold is 0.3.

Method	Reconstruction Accuracy %			Pose Accuracy %				Motion Accuracy %				Overall Accuracy %		
	Object@0.5	Moving@0.5	AccR	Rot@10	Trans@0.5	Scale@0.3	AccP	O@0.5	OA@10	OAD@10	AccM @10	AccRP	RPOA	AccRPM
3DADN [31]	1.0	38.6	1.0	2.8	0.7	8.5	0.0	15.3	7.8	4.4	0.0	0.0	0.0	0.0
CUBERAND	8.7	10.6	1.0	0.3	0.8	43.2	0.0	0.0	0.0	0.0	0.0	0.0	0.0	0.0
CUBEOPT *	35.5	65.5	29.5	19.2	1.7	62.9	1.0	43.9	20.1	16.3	10.0	1.0	0.7	0.5
D3DHOI-GT-CAD [44]*	76.0	90.1	74.3	44.7	41.8	86.8	33.9	84.9	59.8	59.8	38.7	33.4	33.3	25.2
D3DHOI-Rand-Cat-CAD*	64.5	75.9	51.9	35.1	23.5	83.1	18.4	73.6	42.7	41.8	22.4	16.1	15.1	9.9
D3DHOI-Rand-CAD*	38.8	60.7	26.2	20.8	8.2	77.2	5.9	59.8	18.8	13.4	5.7	4.4	2.7	1.8
DITTO [19]	45.3	15.6	6.4	60.7	17.1	97.8	10.5	91.1	3.5	0.4	0.0	0.7	0.0	0.0
LASR [45]*	14.1	5.6	1.3	4.1	0.0	38.7	0.0	0.0	0.0	0.0	0.0	0.0	0.0	0.0
ViSER [46]*	7.9	7.3	0.1	5.4	0.0	0.5	0.0	0.0	0.0	0.0	0.0	0.0	0.0	0.0

articulated object and its parts, we compute the Chamfer Distance (CD) between 10000 sampled surface points from the estimated 3D representation and the ground truth. Since our goal for this metric is to measure reconstruction quality, we factor out pose by normalizing the scale of both the predicted mesh and the ground truth mesh by their maximum dimension. We then apply ICP [1] to align the two meshes. This allows us to use the CD metric to capture the reconstruction error. We also measure the CD for both the entire object and the moving part in isolation. For the accuracy metric, we compute a combined accuracy (AccR) that combines the thresholded reconstruction error accuracy for both the whole object and the moving part.

Pose. The scale normalization and ICP alignment from above are also used to evaluate the object pose. We measure the rotation and translation error based on the prediction-to-ground-truth mesh alignment transformation matrix calculated by ICP. For the rotation error, we calculate the error in degrees between two rotation matrices. For the translation error, we calculate the Euclidean distance. For the scale error, we compute the ratio between the maximum dimension of the ground truth object and the predicted object. If the ratio is larger than 1 we take its inverse. Then we subtract this value from 1 to obtain a relative scale error value in [0, 1]. For the

accuracy metric, we define a combined rotation, translation and scale match accuracy (ACCP).

Motion. We evaluate the error of the predicted motion origin point, motion axis (ignoring direction since parametrizations based on both directions are possible), motion axis with direction, and finally motion state (rotation angle). We compute the angle error for the axis and direction, and the distance to the axis for the origin. Note that the maximum angle error is 90° for the motion axis and 180° for the motion axis direction. We report accuracy metrics for these motion parameters in staggered combinations, starting with motion origin (O), origin+axis (OA), OA+Direction (OAD), and overall motion parameter accuracy including all motion parameters: axis, direction, state error (AccM).

Overall. Finally, we report combined accuracy for reconstruction and pose (AccRP), and combined accuracy for reconstruction, pose, and motion state (AccRPM).

5.3. Implementation Details

For 3DADN [31], D3D-HOI [44], LASR [45], ViSER [46] and DITTO [19] we use the open-sourced implementations provided by the authors to evaluate these methods on our benchmark. For DITTO, we use the pretrained network released by the authors to run inference on our data. We

implement the CuboidOPT method in PyTorch3D [32] and minimize the final objective function using gradient based optimization. We use PyTorch3D’s differentiable renderer to render the object and part masks used to compute the loss functions. We do not assume any ground truth information about the object shape and human-object interaction contact point so the optimization is over all templates and left/right hand combinations for human-object interaction terms. We select the optimization run achieving minimum loss. We use Adam [23] as our optimizer with a learning rate of 0.05 and a decay factor of 10 in the last 25% of the iterations. We optimize each model for a total of 500 iterations.

5.4. Results

We report error metrics for the five types of approaches in Table 1, and thresholded accuracies in Table 2. We also plot accuracies against error threshold for the accuracies in Figure 3. Finally, we show qualitative results in Figure 5. Most of the methods in this comparison have access to privileged information: LASR has access to the ground-truth (GT) object mask for each video frame, and CUBE OPT has access to the GT object and part masks.

How well does free-form mesh fitting work? LASR is the most flexible in shape reconstruction, and gives comparable object CD as CUBE OPT. However, it often has large errors in the pose of the object in camera coordinates. To extract motion parameters from LASR and ViSER outputs, we use the predicted bone weights to obtain a part segmentation of the object. We then extract part boundary vertices and compute the dominant axis direction using PCA. The median of the boundary vertices is used as the origin. We note that ViSER outputs typically have a very different pose compared to GT and therefore struggles more on motion parameter estimation. On the other hand, DITTO performs well on reconstruction and pose parameter estimation. This may be attributed to the fact that DITTO uses GT point clouds.

How much does knowing the ground-truth CAD model help? D3DHOI is the most privileged method with access to the GT object mask and the GT CAD model that captures the shape of the object, the moving part and how it is attached to the static part. There is limited need for reconstruction (though the scale factors σ still need to be estimated). Instead, the problem is reduced to just pose and motion parameter estimation. Unsurprisingly, D3DHOI has the best overall performance (in terms of reconstruction, pose, and motion errors). Reconstruction is still not perfect due to errors in estimating the scale parameters of the CAD model. For a fairer comparison, we also consider fetching a random model (over all models vs using one with the GT category). Performance deteriorates but is still fairly high for the D3DHOI-Rand-Cat-CAD as there is a limited number of models to sample from (24 overall, and on average about

two given the category). D3DHOI-Rand-CAD is comparable to CUBE OPT, better on some metrics (moving part CD, pose rotation and translation), while worse on others (motion prediction).

How well can naïve cuboidal approximation of object shape work? We also evaluate CUBERAND, a “random” baseline based on CUBE OPT with random initialization. Note that this is stronger than a purely random baseline as CUBE OPT already has inductive biases due to the prior knowledge of the template structures that are built-in. While CUBERAND performs worse than the other methods in most of the error metrics, the pose error is actually similar to that of the optimized CUBE OPT and D3DHOI-Rand-CAD, indicating that a simple approximation with two cuboids captures the articulated object fairly well. From the accuracy results (Table 2), the weakness of this random baseline becomes more obvious, as it has extremely low accuracy on object reconstruction, pose rotation/translation, and zero accuracy on motion prediction metrics. The supplement provides additional ablations that investigate the impact of the loss terms in the CUBE OPT approach.

What if we used a plane approximation and had no access to GT object masks? 3DADN is given the least information. It is the only approach that does not assume access to the GT object mask. However, it can only model the moving part, so it has the highest object-level CD, but relatively low CD for the moving part. The pose error is also the highest of the methods, and motion error is also relatively high. 3DADN does not predict the motion state (i.e. rotation angle) for every frame as its temporal optimization algorithm selects subsets of frames from the input. We report the errors on the subset of the frames with predicted motion parameters.

How challenging are different object categories? Figure 4 shows a category-wise breakdown of the reconstruction accuracy metric for each method. Overall, laptops are most challenging (likely because the moving part is relatively small), while dishwashers are easiest (relatively large object and large moving part). CUBE OPT works much better for microwaves than D3DHOI (good fit with two-cuboid assumption). Both methods do well on dishwashers, but less well on ovens (the bottom proofing drawer likely makes the articulation edge not as clear for ovens).

What if we use predicted object masks for CUBE OPT? We also experiment with predicted object and part masks for CUBE OPT. Specifically, we compare using ground-truth (GT) vs predicted (Pred) object and part masks. We use the predicted part segmentation from 3DADN to as the moving part mask. For the object mask, we use Mask2Former [7] (Swin Large trained on COCO). Since the pretrained Mask2Former on COCO does not include all the categories for D3DHOI, we only evaluate on 4 categories

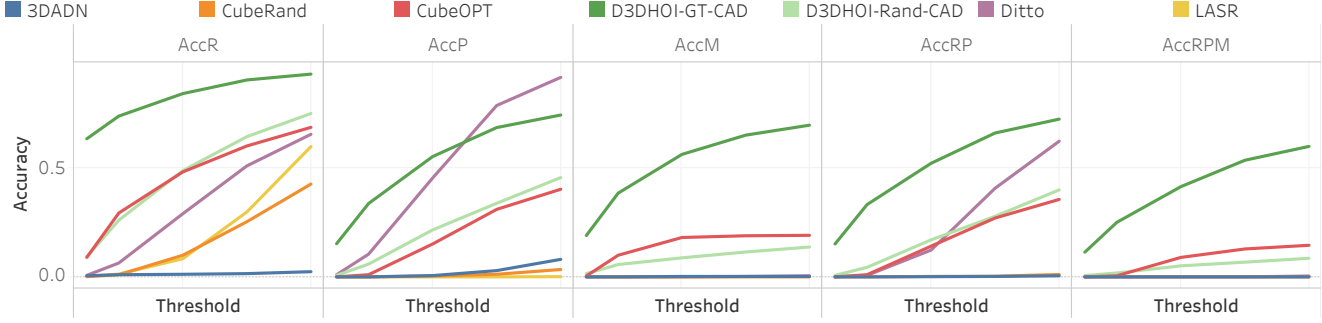


Figure 3. Accuracy of reconstruction (AccR), pose (AccP), motion (AccM), reconstruction+pose (AccRP), reconstruction+pose+motion (AccRPM) at varying thresholds: $< 0.25, 0.5, 1.0, 1.5, 2.0$ for reconstruction (CD) and axis origin error, $< 0.2, 0.3, 0.4, 0.5, 0.6$ for scale error, $< 5, 10, 15, 20, 25^\circ$ for angle error (pose rotation, motion parameters). As the threshold is increased, the strictness of the condition for a prediction to be correct is relaxed, and the accuracy increases. D3DHOI-GT-CAD which relies on having the GT CAD model in addition to the GT object mask has the best overall performance. The cuboidal abstraction method CUBEOPT has access to the GT object and part image mask, and the free-form mesh fitting LASR has access to the GT object mask. The latter is able to reconstruct the object somewhat but ends up underperforming the randomly initialized CUBEOPT, showing that having a cuboidal assumption is helpful for many articulated objects. DITTO has access to GT point clouds of the objects and therefore outperforms all other baselines in pose estimation. 3DADN is a 2D method that does not have access to GT information and leverages pretraining on large amounts of internet videos. Since it models only the moving part, it cannot reconstruct the static part and has poor overall reconstruction performance. All methods other than CUBEOPT and D3DHOI are unable to predict the combined motion parameters, and overall pose, indicating the significant challenges of this task.

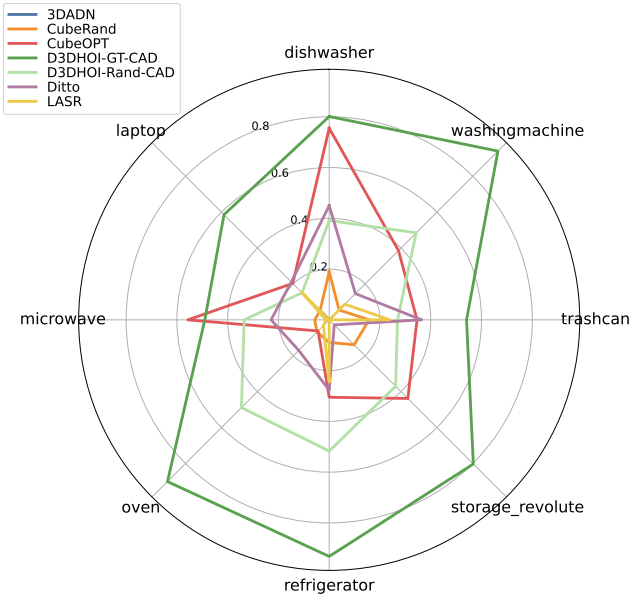


Figure 4. Category-wise breakdown of the reconstruction accuracy metric (AccR) for all methods in our experiments. The microwave, laptop, and trashcan are overall most challenging for most methods. 3DADN is at zero in almost all categories except laptop and therefore not visible.

(laptop, microwave, oven, refrigerator) from the original dataset (170 videos). We compare CUBEOPT-Pred with 3DADN for these 170 videos, and find that CUBEOPT achieves lower error and higher accuracy (see supplement).

Discussion. Overall, the results indicate that this is a challenging problem with much space for improvement. All

methods, despite having access to GT information, have fairly high motion axis and direction errors and motion state errors. Some predictions are very good, but there are many poor results even within a single video input (as is indicated by the relatively high standard error margins on the reported mean error values in Table 1).

While fairly simple and limited in terms of object shapes it can model CUBEOPT reconstructs the object without needing a CAD model dataset. The built-in bias towards cuboidal part articulated objects helps it outperform 3DADN which similarly does not rely on a database of 3D CAD models, unlikely D3DHOI.

6. Conclusion

In this paper we defined a canonicalized articulated 3D human-object interaction task: single-view reconstruction of objects from RGB videos of humans interacting with an articulated object. We carried out a systematic benchmark of five classes of methods for this task. Using a set of metrics to evaluate the predicted object reconstruction, pose, and motion we saw that all methods struggle to obtain high quality results even when provided with privileged information such as ground truth object masks and CAD models. We see a number of opportunities for future work on improved methods for articulated 3D human-object interaction.

Acknowledgements: This work was funded in part by a Canada CIFAR AI Chair, a Canada Research Chair and NSERC Discovery Grant, and enabled in part by support from [WestGrid](#) and [Compute Canada](#). We thank Xiang Xu, Shengyi Qian and Zhenyu Jiang for answering questions



Figure 5. Qualitative comparison of methods on several example videos. Obtaining high accuracy results for articulated 3D human-object interaction is quite challenging. All approaches (other than 3DADN) are given ground-truth object segmentation masks but still exhibit significant errors in object shape reconstruction (in particular 3DADN which only handles the moving part of the object), and in motion parameter estimation (in particular CUBEOPT which gets the motion axis wrong in the second to last row from the bottom). The LASR approach often struggles to estimate a reliable pose for the reconstructed object.

about D3DHOI, 3DADN and Ditto respectively.

References

- [1] K Somani Arun, Thomas S Huang, and Steven D Blostein. Least-squares fitting of two 3-D point sets. *Transactions on Pattern Analysis and Machine Intelligence (TPAMI)*, 1987. 5
- [2] Trevor Bergstrom and Humphrey Shi. Human-object interaction detection: A quick survey and examination of methods. In *Proceedings of the 1st International Workshop on Human-centric Multimedia Analysis*, pages 63–71, 2020. 2
- [3] Bharat Lal Bhatnagar, Xianghui Xie, Ilya A Petrov, Cristian Sminchisescu, Christian Theobalt, and Gerard Pons-Moll. BEHAVE: Dataset and method for tracking human object interactions. In *Conference on Computer Vision and Pattern Recognition (CVPR)*, 2022. 1, 2
- [4] Benjamin Biggs, Thomas Roddick, Andrew Fitzgibbon, and Roberto Cipolla. Creatures great and small: Recovering the shape and motion of animals from video. In *Asian Conference on Computer Vision*, pages 3–19. Springer, 2018. 2
- [5] Federica Bogo, Angjoo Kanazawa, Christoph Lassner, Peter Gehler, Javier Romero, and Michael J Black. Keep it SMPL: Automatic estimation of 3D human pose and shape from a single image. In *European Conference on Computer Vision (ECCV)*, pages 561–578. Springer, 2016. 1
- [6] Zhe Cao, Ilija Radosavovic, Angjoo Kanazawa, and Jitendra Malik. Reconstructing hand-object interactions in the wild. In *International Conference on Computer Vision (ICCV)*, pages 12417–12426, 2021. 2
- [7] Bowen Cheng, Alexander G. Schwing, and Alexander Kirillov. Per-pixel classification is not all you need for semantic segmentation. In *Advances in Neural Information Processing Systems (NeurIPS)*, 2021. 6, 12
- [8] Angela Dai, Angel X Chang, Manolis Savva, Maciej Halber, Thomas Funkhouser, and Matthias Nießner. ScanNet: Richly-annotated 3D reconstructions of indoor scenes. In *Conference on Computer Vision and Pattern Recognition (CVPR)*, pages 5828–5839, 2017. 3
- [9] Haoqiang Fan, Hao Su, and Leonidas J Guibas. A point set generation network for 3D object reconstruction from a single image. In *Conference on Computer Vision and Pattern Recognition (CVPR)*, pages 605–613, 2017. 4
- [10] Zicong Fan, Omid Taheri, Dimitrios Tzionas, Muhammed Kocabas, Manuel Kaufmann, Michael J Black, and Otmar Hilliges. Articulated objects in free-form hand interaction. *arXiv:2204.13662*, 2022. 2
- [11] Matthew Fisher, Manolis Savva, Yangyan Li, Pat Hanrahan, and Matthias Nießner. Activity-centric scene synthesis for functional 3d scene modeling. *ACM Transactions on Graphics (TOG)*, 34(6):1–13, 2015. 2
- [12] Mohamed Hassan, Partha Ghosh, Joachim Tesch, Dimitrios Tzionas, and Michael J Black. Populating 3D scenes by learning human-scene interaction. In *Conference on Computer Vision and Pattern Recognition (CVPR)*, pages 14708–14718, 2021. 2
- [13] Yana Hasson, Gul Varol, Dimitrios Tzionas, Igor Kalevatykh, Michael J Black, Ivan Laptev, and Cordelia Schmid. Learning joint reconstruction of hands and manipulated objects. In *Conference on Computer Vision and Pattern Recognition (CVPR)*, pages 11807–11816, 2019. 2
- [14] Kaiming He, Georgia Gkioxari, Piotr Dollár, and Ross Girshick. Mask R-CNN. In *International Conference on Computer Vision (ICCV)*, pages 2961–2969, 2017. 3
- [15] Umar Iqbal, Kevin Xie, Yunrong Guo, Jan Kautz, and Pavlo Molchanov. KAMA: 3D keypoint aware body mesh articulation. In *International Conference on 3D Vision (3DV)*, pages 689–699. IEEE, 2021. 1
- [16] Ajinkya Jain, Rudolf Lioutikov, Caleb Chuck, and Scott Niekum. ScrewNet: Category-independent articulation model estimation from depth images using screw theory. In *International Conference on Robotics and Automation (ICRA)*, pages 13670–13677. IEEE, 2021. 2
- [17] Ajinkya Jain, Stephen Giguere, Rudolf Lioutikov, and Scott Niekum. Distributional depth-based estimation of object articulation models. In *Conference on Robot Learning (CoRL)*, pages 1611–1621. PMLR, 2022. 2
- [18] Yun Jiang, Hema S Koppula, and Ashutosh Saxena. Modeling 3D environments through hidden human context. *Transactions on Pattern Analysis and Machine Intelligence (TPAMI)*, 38(10):2040–2053, 2015. 2
- [19] Zhenyu Jiang, Cheng-Chun Hsu, and Yuke Zhu. Ditto: Building digital twins of articulated objects from interaction. In *Conference on Computer Vision and Pattern Recognition (CVPR)*, 2022. 2, 4, 5, 12
- [20] Hanbyul Joo, Natalia Neverova, and Andrea Vedaldi. Exemplar fine-tuning for 3D human pose fitting towards in-the-wild 3D human pose estimation. In *International Conference on 3D Vision (3DV)*, 2021. 4
- [21] Angjoo Kanazawa, Jason Y Zhang, Panna Felsen, and Jitendra Malik. Learning 3D human dynamics from video. In *Conference on Computer Vision and Pattern Recognition (CVPR)*, pages 5614–5623, 2019. 2
- [22] Tero Karras. Maximizing parallelism in the construction of BVHs, octrees, and k-d trees. In *Proceedings of the ACM SIGGRAPH/Eurographics conference on High-Performance Graphics*, pages 33–37, 2012. 11
- [23] Diederik P Kingma and Jimmy Ba. Adam: A method for stochastic optimization. *arXiv:1412.6980*, 2014. 6
- [24] Xiaolong Li, He Wang, Li Yi, Leonidas J Guibas, A Lynn Abbott, and Shuran Song. Category-level articulated object pose estimation. In *Conference on Computer Vision and Pattern Recognition (CVPR)*, pages 3706–3715, 2020. 2
- [25] Qihao Liu, Weichao Qiu, Weiyao Wang, Gregory D Hager, and Alan L Yuille. Nothing but geometric constraints: A model-free method for articulated object pose estimation. *arXiv:2012.00088*, 2020. 2
- [26] Matthew Loper, Naureen Mahmood, Javier Romero, Gerard Pons-Moll, and Michael J Black. SMPL: A skinned multi-person linear model. *ACM Transactions on Graphics (TOG)*, 34(6):1–16, 2015. 1, 4
- [27] Frank Michel, Alexander Krull, Eric Brachmann, Michael Ying Yang, Stefan Gumhold, and Carsten Rother. Pose estimation of kinematic chain instances via object coordinate regression. In *British Machine Vision Conference (BMVC)*, pages 181–1, 2015. 2
- [28] Jiteng Mu, Weichao Qiu, Adam Kortylewski, Alan Yuille,

- Nuno Vasconcelos, and Xiaolong Wang. A-SDF: Learning disentangled signed distance functions for articulated shape representation. In *International Conference on Computer Vision (ICCV)*, 2021. 2, 4
- [29] Atsuhiro Noguchi, Umar Iqbal, Jonathan Tremblay, Tatsuya Harada, and Orazio Gallo. Watch it move: Unsupervised discovery of 3D joints for re-posing of articulated objects. In *Conference on Computer Vision and Pattern Recognition (CVPR)*, 2022. 2
- [30] Georgios Pavlakos, Vasileios Choutas, Nima Ghorbani, Timo Bolkart, Ahmed AA Osman, Dimitrios Tzionas, and Michael J Black. Expressive body capture: 3D hands, face, and body from a single image. In *Conference on Computer Vision and Pattern Recognition (CVPR)*, pages 10975–10985, 2019. 1
- [31] Shengyi Qian, Linyi Jin, Chris Rockwell, Siyi Chen, and David F Fouhey. Understanding 3D object articulation in internet videos. In *Conference on Computer Vision and Pattern Recognition (CVPR)*, 2022. 1, 2, 3, 5, 12
- [32] Nikhila Ravi, Jeremy Reizenstein, David Novotny, Taylor Gordon, Wan-Yen Lo, Justin Johnson, and Georgia Gkioxari. Accelerating 3d deep learning with pytorch3d. *arXiv:2007.08501*, 2020. 6
- [33] Manolis Savva, Angel X Chang, Pat Hanrahan, Matthew Fisher, and Matthias Nießner. Pigraphs: learning interaction snapshots from observations. *ACM Transactions on Graphics (TOG)*, 35(4):1–12, 2016. 2
- [34] Jürgen Sturm, Vijay Pradeep, Cyrill Stachniss, Christian Plagemann, Kurt Konolige, and Wolfram Burgard. Learning kinematic models for articulated objects. In *International Joint Conference on Artificial Intelligence (IJCAI)*, 2009. 2
- [35] Jürgen Sturm, Cyrill Stachniss, and Wolfram Burgard. A probabilistic framework for learning kinematic models of articulated objects. *Journal of Artificial Intelligence Research*, 41:477–526, 2011. 2
- [36] Wei-Cheng Tseng, Hung-Ju Liao, Lin Yen-Chen, and Min Sun. CLA-NeRF: Category-level articulated neural radiance field. *arXiv:2202.00181*, 2022. 2
- [37] Aggeliki Tsoli and Antonis A Argyros. Joint 3D tracking of a deformable object in interaction with a hand. In *European Conference on Computer Vision (ECCV)*, pages 484–500, 2018. 2
- [38] Dimitrios Tzionas, Luca Ballan, Abhilash Srikantha, Pablo Aponte, Marc Pollefeys, and Juergen Gall. Capturing hands in action using discriminative salient points and physics simulation. *International Journal of Computer Vision*, 118(2):172–193, 2016. 11
- [39] He Wang, Srinath Sridhar, Jingwei Huang, Julien Valentin, Shuran Song, and Leonidas J Guibas. Normalized object coordinate space for category-level 6D object pose and size estimation. In *Conference on Computer Vision and Pattern Recognition (CVPR)*, pages 2642–2651, 2019. 4
- [40] Xiaogang Wang, Bin Zhou, Yahao Shi, Xiaowu Chen, Qinping Zhao, and Kai Xu. Shape2motion: Joint analysis of motion parts and attributes from 3d shapes. In *Conference on Computer Vision and Pattern Recognition (CVPR)*, pages 8876–8884, 2019. 4
- [41] Shangzhe Wu, Tomas Jakab, Christian Rupprecht, and Andrea Vedaldi. DOVE: Learning deformable 3D objects by watching videos. *arXiv:2107.10844*, 2021. 1, 2
- [42] Yu Xiang, Tanner Schmidt, Venkatraman Narayanan, and Dieter Fox. PoseCNN: A convolutional neural network for 6D object pose estimation in cluttered scenes. In *Proceedings of Robotics: Science and Systems (RSS)*, 2017. 4
- [43] Xianghui Xie, Bharat Lal Bhatnagar, and Gerard Pons-Moll. CHORE: Contact, human and object reconstruction from a single RGB image. *arXiv:2204.02445*, 2022. 1, 2
- [44] Xiang Xu, Hanbyul Joo, Greg Mori, and Manolis Savva. D3D-HOI: Dynamic 3D human-object interactions from videos. *arXiv:2108.08420*, 2021. 1, 2, 3, 4, 5, 11, 12
- [45] Gengshan Yang, Deqing Sun, Varun Jampani, Daniel Vlasic, Forrester Cole, Huiwen Chang, Deva Ramanan, William T Freeman, and Ce Liu. LASR: Learning articulated shape reconstruction from a monocular video. In *Conference on Computer Vision and Pattern Recognition (CVPR)*, pages 15980–15989, 2021. 1, 2, 4, 5
- [46] Gengshan Yang, Deqing Sun, Varun Jampani, Daniel Vlasic, Forrester Cole, Ce Liu, and Deva Ramanan. ViSER: Video-specific surface embeddings for articulated 3D shape reconstruction. *Advances in Neural Information Processing Systems*, 34, 2021. 4, 5
- [47] Gengshan Yang, Minh Vo, Natalia Neverova, Deva Ramanan, Andrea Vedaldi, and Hanbyul Joo. Banmo: Building animatable 3d neural models from many casual videos. In *Proceedings of the IEEE/CVF Conference on Computer Vision and Pattern Recognition*, pages 2863–2873, 2022. 1, 2
- [48] Jason Y Zhang, Sam Pepose, Hanbyul Joo, Deva Ramanan, Jitendra Malik, and Angjoo Kanazawa. Perceiving 3D human-object spatial arrangements from a single image in the wild. In *European Conference on Computer Vision (ECCV)*, pages 34–51. Springer, 2020. 1, 2
- [49] Silvia Zuffi, Angjoo Kanazawa, David W Jacobs, and Michael J Black. 3D menagerie: Modeling the 3D shape and pose of animals. In *Conference on Computer Vision and Pattern Recognition (CVPR)*, pages 6365–6373, 2017. 1
- [50] Silvia Zuffi, Angjoo Kanazawa, and Michael J Black. Lions and tigers and bears: Capturing non-rigid, 3D, articulated shape from images. In *Conference on Computer Vision and Pattern Recognition (CVPR)*, pages 3955–3963, 2018.
- [51] Silvia Zuffi, Angjoo Kanazawa, Tanya Berger-Wolf, and Michael J Black. Three-D safari: Learning to estimate zebra pose, shape, and texture from images “in the wild”. In *International Conference on Computer Vision (ICCV)*, pages 5359–5368, 2019. 1

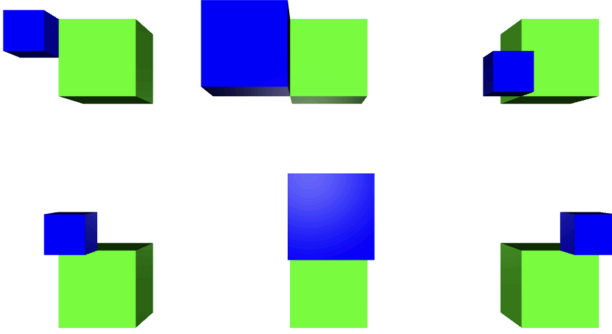


Figure 6. Example CUBEOPT initialization templates for the left edge (top row) and for the top edge (bottom row). For each edge, the moving part (blue cuboid) is attached at half length constrained to touch one end of the edge, full length spanning the edge, or half length touching the other end of the edge.

This supplemental document provides the following additional content to support the main paper:

- A** : implementation details for the CUBEOPT method.
- B** : details of method based on DITTO.
- C** : additional qualitative result examples.
- D** : additional quantitative evaluations and ablations.

A. CUBEOPT implementation details

Initializations. Estimating a cuboid abstraction from 2D images is an underconstrained problem. Thus, we design a set of “templates” that serve as initializations. We first initialize the base part to be in the center of the image. Then for each of up to four edges that are visible from the camera, we attach the moving part to the edge in three possible configurations. The moving part is scaled to be: i) the full length of the edge; or ii) half the length and starting from one end of the edge; or iii) half the length and starting from the other end. Figure 6 shows example templates for two edges. This scheme leads to a total of 12 possible templates that are used as initializations. We run CUBEOPT over all these initializations and select the best result.

Objective Functions. We estimate the rotation, translation, scale and articulation parameters by optimizing an objective function which is a sum of a silhouette loss (L_{sil}) and a Dice loss (L_{dice}) for ensuring the ground truth and projected 3D object masks are the same, an overlap loss (L_{over}) to penalize interpenetration of the cuboids, and a human-object interaction loss (L_{hoi}).

Silhouette loss L_{sil} : penalizes the discrepancy between the ground truth object mask, M_t^{gt} and the projected 3D object mask M_t^{proj} . We project the object into a 2D image mask at each frame time t to compute the loss as a mean of

the discrepancies,

$$L_{\text{sil}}(M_t^{\text{gt}}, M_t^{\text{proj}}) = \frac{1}{N} \sum_{t=1}^N \|M_t^{\text{gt}} - M_t^{\text{proj}}\|_2^2 \quad (1)$$

We apply this loss over the full object, base part and moving part separately i.e. the loss is defined as,

$$L_{\text{sil}} = L_{\text{sil}}^{\text{obj}} + L_{\text{sil}}^{\text{base}} + L_{\text{sil}}^{\text{move}} \quad (2)$$

Dice loss L_{dice} : maximizes intersection-over-union (IoU) between ground truth object mask M_t^{gt} and projected 3D object mask M_t^{proj} . The loss is computed over all frames as,

$$L_{\text{dice}}(M_t^{\text{gt}}, M_t^{\text{proj}}) = \frac{1}{N} \sum_{t=1}^N 1 - \text{IoU}(M_t^{\text{gt}}, M_t^{\text{proj}}) \quad (3)$$

Similarly to the silhouette loss, we also apply the Dice loss over full object, base part and moving part separately,

$$L_{\text{dice}} = L_{\text{dice}}^{\text{obj}} + L_{\text{dice}}^{\text{base}} + L_{\text{dice}}^{\text{move}} \quad (4)$$

Overlap loss L_{over} : penalizes overlap between the two cuboids C_b and C_m . This is used to discourage degenerate solutions where both the cuboids have significant overlap to the point where only one cuboid is visible in the projection. We adopt a mesh-mesh overlap term from prior work to detect colliding mesh triangles and penalize the depth of the penetration of the collisions [22, 38].

Human-object interaction loss L_{hoi} : consists of a “depth loss” to encourage the depth of the human and the object to be similar, and a “contact curve loss” to encourage the moving part to move along with the human contact point. The former is implemented by minimizing the difference between the average z -component of the human and object mesh vertices. The latter is adapted from Xu et al. [44]’s contact curve loss to constrain the moving part of the object to follow a similar curve as the human hand.

The L_{hoi} loss is composed of two terms: L_{depth} and L_{contact} .

For the L_{depth} term, since we know that the human and object are always in front of the camera, we use the z coordinates of the human and object mesh vertices as a proxy for depth from the camera. We define this term as the difference between the mean z coordinate of the vertices of the human and object meshes.

$$L_{\text{depth}} = \max(0, \left| \frac{1}{N} \sum_i^N H_i^z - \frac{j}{M} \sum_j^M S_j^z \right| - \lambda)$$

where H_i^z is the z -component of the i -th vertex of the human mesh and similarly, S_j^z is the z -component of the j -th vertex of the object mesh and λ is a threshold parameter which we set to 0.1 in our experiments.

For the L_{contact} term, we adapt the contact curve loss from Xu et al. [44] which constrains the moving part of the object to follow a similar curve as the human hand. We select the centroid of the moving part at each timestep t , $v_c(t)$, as our contact point on the object and the centroid of a hand of the human at each timestep, $h_c(t)$, as the contact point on the human. Note that the human pose estimates are “jittery” and therefore it is difficult to get a consistent contact point estimate. This is why we resort to the centroid of the moving part as our contact point to mitigate some of the pose estimation noise. Also, we are more concerned with the trajectory of the motion than accurate contact point estimates. Following Xu et al. [44], we allow for a rigid transformation of $v_c(t)$ so that the contact loss focuses only on the shape of the curve. The contact curve loss is then defined as,

$$L_{\text{contact}} = \sum_{t=1}^{t=N} (R_c v_c(t) + T_c - h_c(t))^2$$

Here, R_c and T_c are rotation and translation parameters that we optimize for the contact curve.

Final objective function: a sum of all the loss terms described above,

$$L_{\text{final}} = L_{\text{sil}} + L_{\text{dice}} + L_{\text{over}} + L_{\text{hoi}} \quad (5)$$

B. Details of method based on DITTO

There are a number of key differences in how we use DITTO [19] compared to the original paper. These differences may result in poorer performance when applied to our scenario. 1) In the DITTO paper, the input point clouds are obtained by fusing multi-view depth images, but may still suffer from incompleteness due to self-occlusion (e.g., part of the object is not visible such as a drawer of a cabinet in the closed state). Note that this is different from the incompleteness of the single-view point clouds with which we work. 2) The pretrained model is trained with the world coordinates matching the canonical object coordinate. Thus, there is an implicit assumption that points are in canonical object coordinate. Note that this differs from our use case, where we do not have the canonical object coordinates. 3) We apply the DITTO model on a full video sequence vs just two point clouds. For some frames, the articulation state w.r.t. the reference closed state may be too similar, causing the network to perform badly. 4) Our videos contain a human interacting with the object, which can result in additional occlusions.

C. Additional qualitative examples

Figure 7 shows further examples of the reconstruction quality achieved by the methods we benchmarked. As we

saw in the main paper, all approaches make significant errors in reconstruction and motion parameter estimation. Due to the severely under-constrained nature of this problem, even methods with ground truth information struggle to reconstruct the objects reliably. Specifically, CUBEOPT often makes error in motion axis and motion state parameter estimation. D3DHOI which has access to ground truth cad models also struggles to estimate the pose in many scenarios (trash bin in first row, and cabinet in second to last row).

D. Additional quantitative evaluation

CUBEOPT ablations. We experiment with different versions of the CUBEOPT baseline (see Table 3 and Table 4). Here, we report numbers for different configurations of the losses used in CUBEOPT. We start with all the losses and then ablate the components of L_{hoi} . We note that L_{contact} helps achieve much better reconstruction and pose results and L_{depth} leads to better performance on Scale and Origin estimates.

We also investigate the use of ground-truth (GT) and predicted (Pred) object and part masks. For predicted masks, we use Mask2Former [7] (Swin Large, trained on COCO) to predict the object masks. Since the pretrained Mask2Former on COCO does not include all the categories for the D3D-HOI dataset we used, we only evaluate on 4 categories (laptop, microwave, oven, refrigerator). For the moving part masks, we use the 3DADN mask estimates without any temporal optimization. Table 3 shows that CUBEOPT performs much worse on predicted masks than ground truth masks. It performs worse for reconstruction and pose error, however it performs close to the ground truth masks baseline on the motion estimates. We also note that CUBEOPT with predicted masks performs similar to random initialization on some metrics showing that there is much room for improvement.

CUBEOPT comparison with 3DADN. 3DADN [31] works by first detecting moving part planes in 2D images and then performing temporal optimization to predict motion parameters including axis and state. We note that the temporal optimization step in 3DADN is analogous to CUBEOPT optimization. Therefore, we compare the results of 3DADN and CUBEOPT with predicted moving part masks. The results are shown in Table 5 and Table 6. We note that CUBEOPT generally outperforms 3DADN including across almost all metrics in Table 6. This shows that an optimization approach with a simple inductive bias of cuboidal abstraction for articulated parts is quite effective, and can compete and outperform a learning-based approach that required large volumes of supervised data.

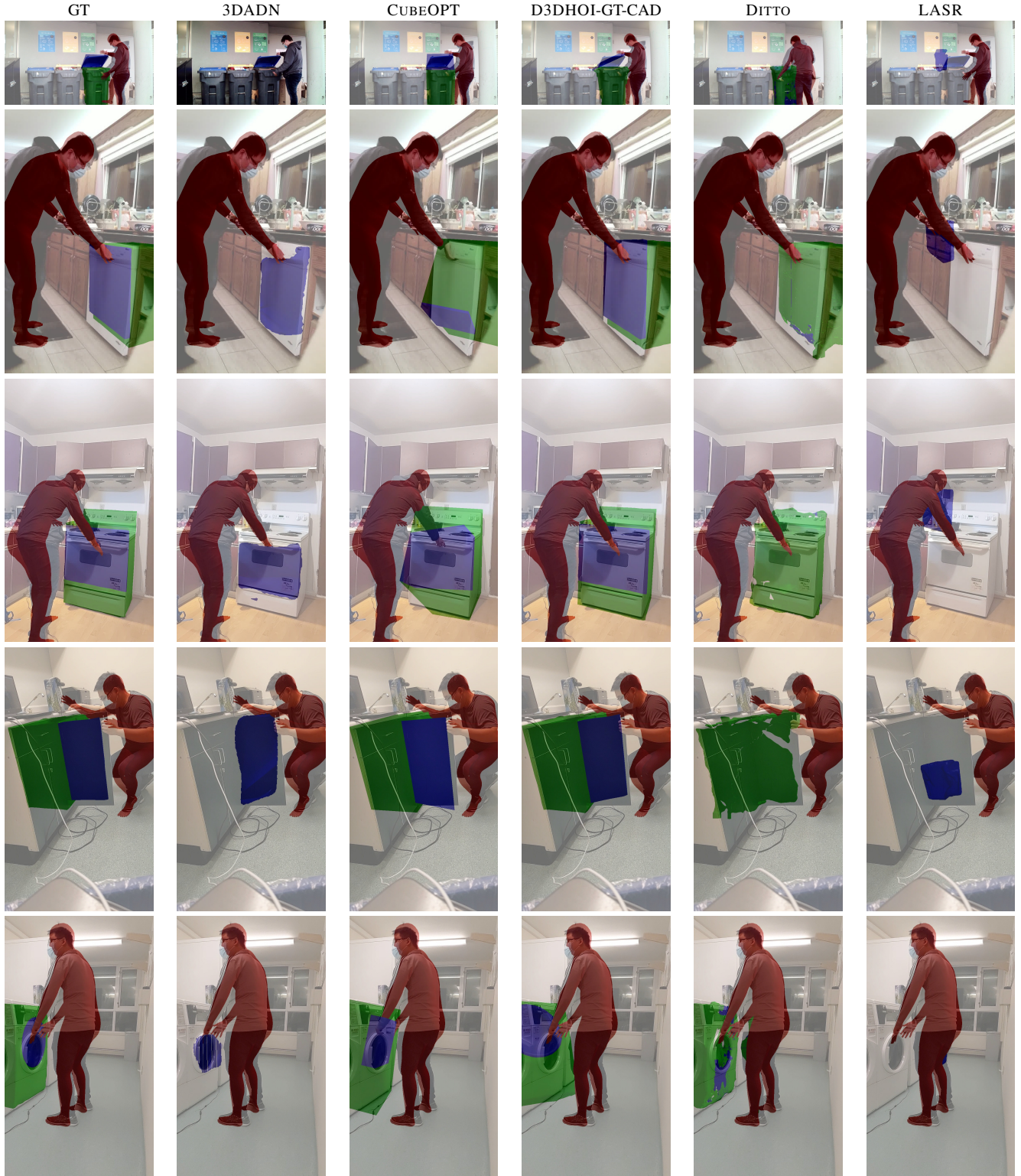


Figure 7. Additional qualitative comparisons. The results show that reconstructing articulated 3D human-object interaction is very challenging. All approaches exhibit significant errors in object shape reconstruction (in particular 3DADN which only handles the moving part of the object), and in motion parameter estimation (in particular CUBEOPT which gets the motion axis wrong in the second and third rows from the top). Even D3DHOI which has access to ground truth CAD models struggles to estimate the correct orientation in the first and last rows.

Table 3. CUBEOPT ablations of ground-truth vs predicted object and part masks, and ablations of human loss terms. Values report mean error for the corresponding estimate.

Mask	Ablation	Reconstruction Error ↓			Pose Error ↓			Motion Error ↓				
		CD (Object)	CD (Moving)		Rotation	Translation	Scale	Origin	Axis	Direction	State	
GT	all losses	1.83 ± 0.15	0.67 ± 0.08	44.19 ± 2.09	2.64 ± 0.12	0.31 ± 0.02	0.72 ± 0.04	24.76 ± 2.38	95.86 ± 5.52	132.01 ± 5.89		
	no L_{depth}	1.06 ± 0.07	0.73 ± 0.09	44.22 ± 2.39	2.58 ± 0.10	0.36 ± 0.01	0.95 ± 0.05	19.44 ± 2.14	101.99 ± 5.75	130.95 ± 6.64		
	no L_{contact}	2.02 ± 0.15	0.68 ± 0.07	46.08 ± 2.25	2.69 ± 0.13	0.35 ± 0.02	0.77 ± 0.04	24.27 ± 2.39	101.32 ± 5.51	147.60 ± 6.26		
	no L_{hoi}	1.14 ± 0.08	0.85 ± 0.10	43.07 ± 2.29	2.58 ± 0.10	0.38 ± 0.02	0.99 ± 0.05	25.95 ± 2.42	96.74 ± 5.46	121.11 ± 6.78		
Pred	all losses	2.15 ± 0.15	0.89 ± 0.09	46.87 ± 2.07	2.67 ± 0.11	0.29 ± 0.02	0.69 ± 0.04	27.46 ± 2.39	91.30 ± 5.36	126.88 ± 5.56		
	no L_{hoi}	1.75 ± 0.12	1.09 ± 0.10	47.56 ± 2.12	2.67 ± 0.09	0.39 ± 0.02	1.15 ± 0.05	40.10 ± 2.72	94.42 ± 4.68	129.95 ± 5.34		
—	CUBERAND	1.40 ± 0.17	1.91 ± 0.01	70.48 ± 6.34	2.10 ± 0.21	0.42 ± 0.02	3.60 ± 0.00	53.25 ± 0.00	122.76 ± 0.00	176.66 ± 40.33		

Table 4. CUBEOPT ablation for ground-truth vs predicted object and part masks, and ablations of human loss terms. Values are accuracies computed at specified error thresholds. The rotation threshold is 10 degree, the translation threshold is 0.5 and the scale threshold is 0.3.

Mask	Ablation	Reconstruction %			Pose %				Motion %				Overall %		
		Object@0.5	Moving@0.5	ACCR	Rot@10	Trans@0.5	Scale@0.3	ACCP	O@0.5	OA@10	OAD@10	AccM@10	ACCRP	RPOA	ACCRPM
GT	all losses	31.8	65.1	26.4	18.0	2.1	56.5	1.4	42.9	21.2	15.9	8.6	1.4	1.0	0.6
	no L_{depth}	33.2	65.6	26.9	20.8	3.4	38.7	1.3	35.3	19.4	17.6	10.6	1.2	1.2	1.2
	no L_{contact}	32.4	66.4	28.5	19.3	3.6	47.0	2.2	39.4	18.2	14.7	8.7	2.2	1.8	0.4
	no L_{hoi}	35.8	62.6	25.9	18.1	1.6	36.6	0.8	27.6	8.8	5.9	2.9	0.6	0.6	0.4
Pred	all losses	21.1	58.4	17.6	14.6	4.5	58.3	2.8	41.8	21.2	15.3	4.4	2.4	2.2	0.8
	no L_{hoi}	21.8	51.5	15.4	12.3	2.2	38.3	0.5	12.9	4.7	1.8	0.5	0.3	0.3	0.1
—	CUBERAND	7.2	9.8	0.8	0.4	0.7	32.4	0.0	0.0	0.0	0.0	0.0	0.0	0.0	0.0

Table 5. Comparison of CUBEOPT using predicted masks vs 3DADN. We use Mask2Former to obtain object masks, and 3DADN to obtain part masks. Since the pretrained Mask2Former on COCO only overlaps in 4 categories (laptop, oven, microwave, refrigerator) with our objects, we evaluate on the subset of videos for these objects (12 videos). CUBEOPT-Pred outperforms 3DADN across all metrics.

Mask	Reconstruction Error ↓			Pose Error ↓			Motion Error ↓				
	CD (Object)	CD (Moving)		Rotation	Translation	Scale	Origin	Axis	Direction	State	
CUBEOPT-Pred	2.153 ± 0.148	0.895 ± 0.091	46.872 ± 2.065	2.670 ± 0.112	0.294 ± 0.015	0.693 ± 0.037	27.457 ± 2.386	91.304 ± 5.357	126.884 ± 5.561		
3DADN	4.041 ± 0.109	0.316 ± 0.038	47.709 ± 1.844	2.009 ± 0.065	0.512 ± 0.015	0.846 ± 0.046	23.549 ± 2.102	111.416 ± 5.443	71.509 ± 19.692		

Table 6. Comparison of CUBEOPT using predicted masks vs 3DADN. We use Mask2Former to obtain object masks, and 3DADN to obtain part masks. Since the pretrained Mask2Former on COCO only overlaps in 4 categories (laptop, oven, microwave, refrigerator) with our objects, we evaluate on the subset of videos for these objects (12 videos). CUBEOPT-Pred outperforms 3DADN across all metrics. The rotation threshold is 10 degree, the translation threshold is 0.5, and the scale threshold is 0.3.

Mask	Reconstruction %			Pose %				Motion %				Overall %		
	Object@0.5	Moving@0.5	ACCR	Rot@10	Trans@0.5	Scale@0.3	ACCP	O@0.5	OA@10	OAD@10	AccM@10	ACCRP	RPOA	ACCRPM
CUBEOPT-Pred	21.1	58.4	17.6	14.6	4.5	58.3	2.8	41.8	21.2	15.3	4.4	2.4	2.2	0.8
3DADN	1.3	45.0	1.3	3.1	0.9	9.0	0.0	17.5	9.7	5.8	0.0	0.0	0.0	0.0